J. Fluid Mech. (1998), *vol.* 364, *pp.* 31–58. Printed in the United Kingdom

Laboratory measurements of the generation and evolution of Langmuir circulations

By W. KENDALL MELVILLE, ROBERT SHEAR AND FABRICE VERON

Scripps Institution of Oceanography, University of California, San Diego, La Jolla, CA 92093-0213, USA

(Received 25 May 1997 and in revised form 27 December 1997)

We present laboratory measurements of the generation and evolution of Langmuir circulations as an instability of a wind-driven surface shear layer. The shear layer, which is generated by an accelerating wind starting from rest above a quiescent water surface, both accelerates and deepens monotonically until the inception of the Langmuir circulations. The Langmuir circulations closely follow the initial growth of the wind waves and rapidly lead to vertical mixing of the horizontal momentum and a deceleration of the surface layer. Prior to the appearance of the Langmuir circulations, the depth of the shear layer scales with $(\nu t)^{1/2}$ (ν is the kinematic viscosity and t is time), in accordance with molecular rather than turbulent transport. For final wind speeds in the range 3 to 5 m s^{-1}, the wavenumber of the most unstable Langmuir circulation normalized by the surface wavenumber, k_{lc}^{*}, is 0.68 ± 0.24, at a reciprocal Langmuir number, La^{-1}, of 52 ± 21. The observations are compared with available theoretical results, although none are directly applicable to the conditions of the experiments. The implications of this work for the generation and evolution of Langmuir circulations in the ocean and other natural water bodies are discussed.

1. Introduction

Long streaks, or 'windrows', are often observed at wind-driven water surfaces, and are believed to be the surface manifestation of subsurface longitudinal vortices which, along with wave breaking, may be responsible for much of the vertical transport in the surface layers of oceans, lakes and other water bodies. The modern literature, which is reviewed by Leibovich (1983), begins with Irving Langmuir's (1938) observation that the streaks were indeed associated with longitudinal counter-rotating vortices roughly aligned with the wind. In recognition of his observations, the phenomenon now bears his name: Langmuir circulations.

A rational theory for the generation of Langmuir circulations (LCs) was proposed by Craik & Leibovich (1976), who showed that a wind-driven surface shear layer, bounded above by an irrotational surface wave field, could become unstable through a so-called vortex force, which is the vector product of the mean Lagrangian velocity, including the Stokes drift due to the waves, and the vorticity. Under the specific Craik–Leibovich II (CLII) mechanism (Craik 1977; Leibovich 1977), a unidirectional surface shear layer with a co-propagating statistically homogeneous wave field may be unstable, leading to the generation of longitudinal vorticity or Langmuir circulations aligned with the wind. Despite numerous field observations (Thorpe & Hall 1983; Weller & Price 1988; Smith 1992; Plueddemann *et al.* 1996) and increasingly

sophisticated numerical solutions of the governing model equations (Leibovich & Paolucci 1980; Skyllingstad & Denbo 1995; McWilliams, Sullivan & Moeng 1997; Leibovich & Yang 1998), the essential predictions of the CLII theory remain unconfirmed by measurements for ocean applications.† A major difficulty has been that for comparison with field data the turbulence has to be parameterized in the CLII model, and our knowledge of surface layer turbulence is at least as poor as that of the LCs (Melville 1996). Furthermore, even some of the more sophisticated large-eddy simulation (LES) models may be subject to numerical artifacts during the initial simulated growth of LCs (Skyllingstad & Denbo 1995). Recent upper-ocean mixing models (Li, Zahariev & Garrett 1995) which attempt to represent the effects of LCs still need to be compared with field data which clearly demonstrate the significance of LCs in developing seas (e.g. Smith 1992).

There is also an instrumentation problem. Modern observations of LCs in the field use side-scan sonars scattering off the bubbles entrained by breaking waves to measure the backscatter strength (Thorpe & Hall 1983), and Doppler techniques to measure the velocity component along the beam (Smith 1992; Farmer & Li 1994; Plueddemann *et al.* 1996). The bubbles are entrained into the convergent downwelling regions of the LCs and this results in enhanced backscatter. The spatial resolution of the Doppler sonars used in this type of measurement has been O(1–10)m, so smaller LCs are not resolved. The dependence on breaking-generated bubbles for scattering restricts the technique to wind speeds greater than approximately 3–6 m s^{-1}. Thus the available measurements may not be well-suited to measuring the initial stages of LC growth in the field; a point made by Smith (1992). Doppler sonars with better spatial resolution could be used, but no single instrument has the range to cover all the expected scales.

Despite the many attempts to produce and measure LCs in the laboratory, success has been confined to those cases in which the water is shallow, and the LCs fill the whole water column (Faller & Caponi 1978). However, determining the vertical and horizontal scales of LCs away from boundaries is one of the primary goals of the theoretical and observational work. Faller & Caponi (1978) have presented qualitative observations which suggested that LCs may be generated following the initiation of a wind, but they did not pursue this in any quantitative way. Kenney (1993) has made qualitative observations of bands of algae in lakes under the influence of very faint breezes, so faint that there was "... generally not enough wind to ripple the lake surface with capillary waves".

The usual scaling of the CLII theory for LC generation in the ocean assumes that the wind-driven surface current is weak ($O(\epsilon)$) compared to the orbital velocity of the surface waves, which in turn is weak ($O(\epsilon)$) compared to the phase speed of the waves: the $O(\epsilon^2)$ theory. This scaling is consistent with fully developed wind waves having phase speeds comparable to the ten-metre wind speed, U_{10}, and surface drift currents $U_s = O(10^{-2}U_{10})$ (Komen *et al.* 1995). However, Craik (1982*a*, *b*) showed that a similar instability mechanism applies if the wind-driven current is of the same order as the phase speed of the waves (the $O(1)$ theory), but now the influence of the LCs on the waves must be considered in a coupled problem. Using the $O(1)$ theory, Phillips & Wu (1994) have numerically solved the eigenvalue problem to study the generation

† In a recent paper Phillips, Wu & Lumley (1996) conclude that laboratory observations of boundary layer flows over rigid wavy terrain by Gong, Taylor & Dörnback (1996) are consistent with the CLII mechanism. However, as noted by Gong *et al.* (1996), their measurements are significantly influenced by the lateral boundaries of the wind tunnel. In any event, their results are not applicable to this oceanographic problem.

of longitudinal vorticity in boundary layers over rigid and air–water boundaries. Phillips & Shen (1996) concluded that this scaling may be more appropriate for the observations of small-scale ($O(10)$cm) LCs in lakes by Kenney (1993). There is no reason to expect that it is only the $O(\epsilon^2)$ scaling that applies to the ocean. The surface wind-drift current U_s is approximately 3% of U_{10}, which is commonly observed up to 15 m s^{-1}, and more in severe storms. So U_s may easily be as large as 50 cm s^{-1} which is the phase speed of 16 cm waves. With the minimum phase speed of irrotational surface waves being 23 cm s^{-1}, wind speeds of 8 m s^{-1} or greater would lead to surface drift currents that match or exceed the minimum phase speed. Phillips, Wu & Jahnke (1997) cite Smith's (1992) field observations of a period in which LCs were absent for 8 m s^{-1} winds, but formed within fifteen minutes of the wind accelerating to 13 m s^{-1}. They interpret these measurements to imply that mean shear in excess of $O(\epsilon^2)$ is necessary for LCs to form. It is not clear that such a strong statement is supported by measurements that could not resolve LCs of scales less than $O(1–10)$m.

We report on laboratory measurements of the generation and evolution of Langmuir circulations following the initiation of the wind. Beginning with a quiescent channel, we show that the wind accelerates a deepening shear layer in the water. The initial absence of surface waves demonstrates that all the momentum flux from the wind is to the surface current. After some time, the surface current becomes unstable to surface wave modes, and very soon thereafter longitudinal vortices (Langmuir circulations) are generated. The initial spacing of the LCs is comparable to the surface wavelength. The LCs rapidly evolve from predominantly two-dimensional structures aligned with the wind to three-dimensional structures through the appearance of bifurcations in the surface jets associated with regions of surface convergence. Through flow visualization of the surface and digital particle imaging velocimetry (DPIV), it is shown that the surface features are associated with regions of concentrated longitudinal vorticity.

In § 2 we describe the experimental procedures and instrumentation. In § 3 we present the main experimental measurements of waves, currents and vorticity along with flow visualization of the surface and interior flows for three wind speeds. In § 4 we compare the measurements with the available predictions of the initial scales of Langmuir circulations according to the CLII theory. In § 5 we discuss the results.

The work reported here was prompted by preliminary qualitative experiments in the large wind-wave channel at Delft Hydraulics in which active infrared imaging and DPIV showed evidence of surface streaks and the instability of the wind-driven current (Haußecker *et al.* 1995). Initial results of the experiments reported here were presented by Melville & Shear (1996).

2. The experiments

The experiments were carried out in the large wind-wave channel in the Hydraulics Laboratory at Scripps Institution of Oceanography. The channel is 45 m long, 2.39 m wide and 2.44 m high. For these experiments the water depth was 1.17 m with the wind-tunnel section occupying the remaining 1.27 m of the channel height. At one end of the channel is a beach and a hydraulically driven fan that draws the air across the water surface, exhausting to the exterior of the laboratory. At the other end of the channel is an entry section for the wind tunnel with a combination of screens and honeycomb sections for flow straightening and conditioning. The overall layout of the facility and the instrumentation is shown in figure 1, with a right-handed coordinate system having the origin in the plane of the mean water level and the x-axis along the centreline of the channel in the direction of the mean wind.

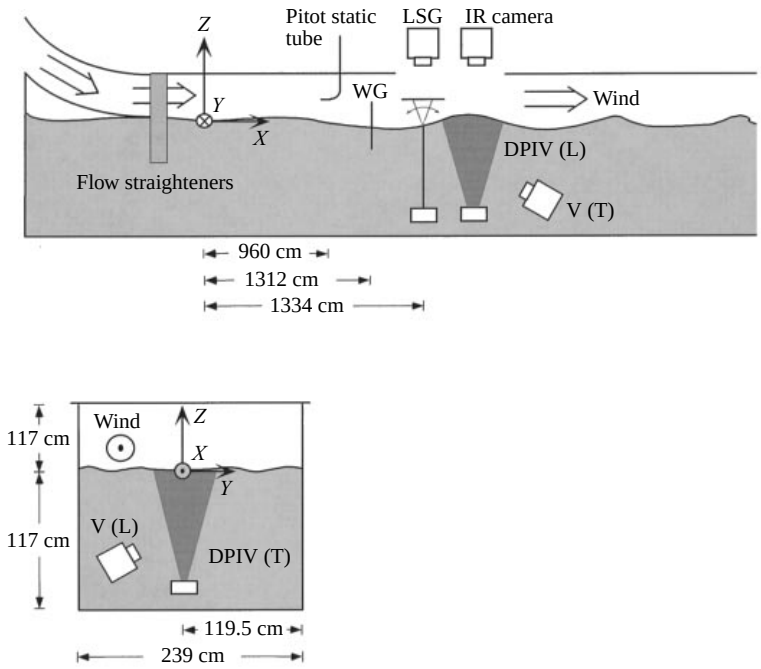

FIGURE 1. A schematic of the experiment and instrumentation in the wind-wave channel at the Hydraulics Laboratory of Scripps Institution of Oceanography. WG denotes wave gauge, LSG laser slope gauge, V video camera, (L) longitudinal and (T) transverse. The LSG, WG and Pitot tube were positioned at $y = 66.2$, 43.3 and 2.5 cm, respectively, at the fetches shown.

The wind speed in the tunnel section was measured with a pitot-static probe connected to a MKS Baratron pressure transducer. The surface waves were measured with fine resistance wire wave gauges, and with a laser slope gauge (LSG). The LSG is a refractive device, with the beam from a laser diode, which is mounted in a waterproof housing under the surface, being refracted at the surface and passing through a Fresnel lens to an imaging screen above the surface. The position of the laser beam on the screen was imaged onto a (UDT Sc10) position photo diode. The device was calibrated to give the surface slope as a function of the position of the laser spot on the screen. For these experiments the LSG measured the component of the wave slope along the channel.

Flow visualization of the surface was accomplished by sprinkling small glass microspheres (3M Company) on the surface, illuminating at grazing incidence from upstream and downstream, and imaging from above with either a video or still camera. Since the scale of the LCs that were initially measured was of O(cm) and since the initial waves generated were in the gravity–capillary range, we were concerned that the particles used for flow visualization could contaminate the surface and modify the results. To check whether this was the case, we used an IR camera (Amber, Radiance 1) to image the surface without particles. The small temperature gradients in the water, which were not of dynamical significance, were sufficient to be able to image the initial stages of LC growth and confirm that the particles had no observable effect on the scale of the LCs. (Due to the small thermal gradients, the contrast of the IR images was not suitable for publication and they are not reproduced here.)

The velocity field in the water was measured using digital particle imaging

velocimetry (DPIV). DPIV, or PIV, may be accomplished with various combinations of hardware and software. The system employed here is based on that described by Willert & Gharib (1991). The flow was seeded with neutrally buoyant Conduct-o-fil silver coated hollow glass particles (Potters Industries, Carlstadt, NJ). The beam from a 5W Argon Ion laser (American Laser Corporation, Salt Lake City, UT, Model 909) passes through a shutter (NM Laser Products, Sunnyvale, CA, Model LS200FNC) which is controlled by a General Pixels DPIV Timer 100. The beam then passes into an optical fibre which is connected to a submersible optical subsystem to generate a light sheet 4 mm wide. The combination of optical fibre and submersible light sheet optics was dictated by the need for accessibility in such a large facility, and for both longitudinal and transverse light sheets for the measurement of velocities in both longitudinal and transverse planes, respectively, relative to the long axis of the channel. A Texas Instruments (TI1134P/GN) CCD camera in a submersible housing could be conveniently positioned in the channel at a sufficient distance from the imaged plane to avoid any significant flow interference. Images from the camera were recorded on a Sony Videodisk Recorder (LVR5000A) for later processing.

The shutter timer, which is synchronized with the camera, generated sequential shutter openings in adjacent camera fields. Correlation processing of the sequential images was then used to calculate the velocity field. The raw velocity data were edited to remove any spurious velocity vectors and interpolated between neighbouring points. The raw velocity vectors were computed on grids of 1.8 mm $\times$ 1.8 mm. Vorticity fields were computed by using the circulation around eight neighbouring points. All DPIV processing was done with a software package developed by Willert & Gharib (1991).

Preliminary experiments without good wind control (Haußecker *et al.* 1995) had shown that LC-like structures followed the initiation of wave generation. Preliminary experiments in the Scripps facility showed that if the wind was turned on too quickly, significant seiching of the channel occurred. In order to avoid this, the wind had to be turned on sufficiently slowly to avoid exciting the normal modes of the channel. This was done in a controlled repeatable fashion by using a computer-controlled hydraulic valve to control the fan speed. It was found that no significant seiching resulted if the wind was accelerated to its constant speed from rest over a period of approximately 20 s. The trigger signal to start the fan provided a consistent time base for ensemble averaging of measurements from repeated experiments. Typically, experiments for each of three final wind speeds of 3, 4 and 5 m s^{-1} were repeated three times.

A sufficient time between runs (15–30 minutes) elapsed for the velocities in the water to settle down to values much less than those associated with the waves, the currents, and the LCs. It is well-known that thermal convection may also give rise to coherent roll structures. The vertical temperature profile was monitored and we were careful to make sure that after filling the channel, sufficient time was allowed for the water temperature to equilibrate with the air temperature. The velocity field at the start of each run was monitored to check for any evidence of thermal convection. None was found.

In a typical experiment the wind was turned on and accelerated to a constant speed over a period of approximately 20 s. Each experiment lasted for 180 s altogether, including approximately 120 s of constant wind speed. Three series of experiments were conducted. The first was for flow visualization using both the IR camera and video imaging of the seeded surface. The second set included wave measurements and velocity measurements in a vertical longitudinal plane. The third set included wave measurements and velocity measurements in a transverse vertical plane.

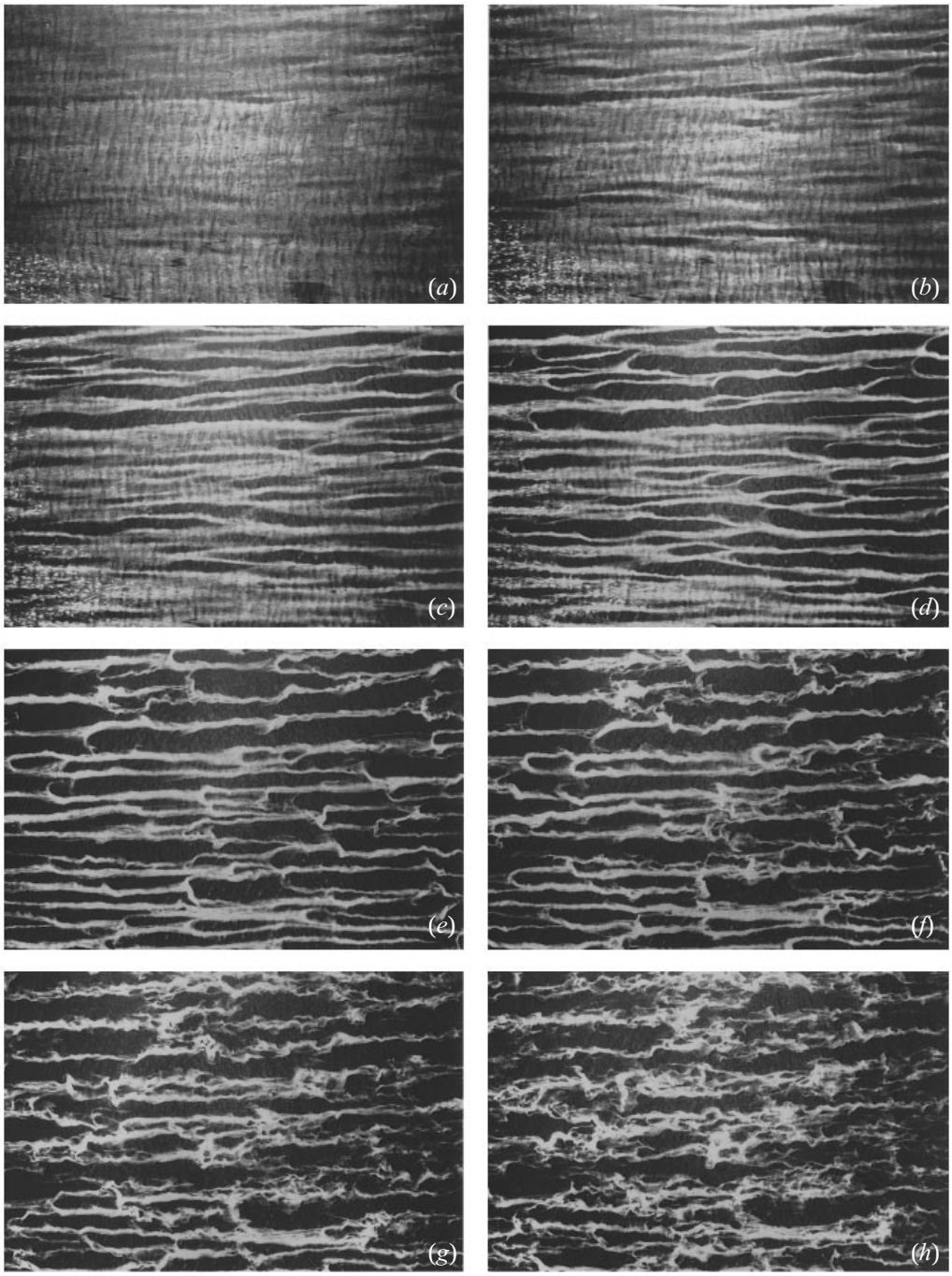

FIGURE 2. Flow visualization of the surface from above for a wind from left to right accelerating to 5 m s^{-1}. Individual frames, which show areas of the surface 85 cm $\times$ 57 cm, are at times $t = 21.5$–25 s from the start of the wind, in 0.5 s increments. The surface was seeded with small glass microspheres and illuminated at grazing incidence with light sources upstream and downstream. The waves travel from left to right and appear as crosswind (vertical) structures in each image, especially in (*a*) to (*d*). The Langmuir circulations appear as predominantly horizontal streaks and undergo several stages in their evolution during the time represented here.

3. Results

3.1. *Flow visualization*

Figure 2 is a sequence of images showing the evolution of the surface signature of Langmuir circulations following the onset of the wind which approaches a final speed of 5 m s^{-1}. The surface was seeded with small slightly buoyant particles and illuminated at grazing incidence from light sources both upstream and downstream. The wind and surface waves move from left to right. The time sequence progresses from left to right and top to bottom at times $t = 21.5$–25 s, at 0.5 s intervals after the initiation of the wind. Each frame size is 85 cm $\times$ 57 cm. LCs are approximately aligned in the horizontal wind direction. At $t = 21.5$ s the surface waves are clearly visible as crosswind (vertical) shadows, and evidence of LCs begins as the divergence of the surface velocity field causes inhomogeneities in the local concentration of particles. At 22–22.5 s the streaks at the surface are clearly evident with particle-free regions beginning to mark areas of surface divergence. At $t = 23$–23.5 s the first signs of significant three-dimensionality develop, but the lines of concentrated particles are still everywhere closely aligned with the mean wind. Bifurcations of the particle streaks become clear and represent regions of strong three-dimensionality where the streaks are locally orthogonal to the wind direction. From observations of video recording, the bifurcations appear to be associated with significant local upwellings and divergence of the velocity field at the surface, with the flow appearing similar to that in the dividing streamline of the two-dimensional flow around a source. At $t = 24$–25 s the particle streaks themselves, which are also regions of enhanced streamwise velocity, develop significant streamwise perturbations, lose some of their coherence, and evolve towards full three-dimensional turbulence. In summary, the four stages progress from initial instability associated with divergence of the transverse velocity field; to quasi-two-dimensional streak formation with large areas almost devoid of particles; then streak dislocation or bifurcation; and finally transition to 'fully' turbulent flow. Generally, the time of inception of the LCs was repeatable to within ± 2 s at the lowest wind speed to ± 1 s at the highest.

Similar stages in the evolution of the surface patterns were found for wind speeds of 3 and 4 m s^{-1}. Figure 3 shows examples of the surface patterns for the three wind speeds at a comparable stage in their evolution (cf. figure 2*d*, *e*); that is, the stage showing streak dislocation or bifurcation. It is clear that an increase in the wind speed leads to a reduction in scale of the streaks. Also, figures 3(*a*) and 3(*b*) show evidence of small-scale surface waves of lengths around 5 cm accompanied by parasitic–capillary waves of centimetre length and less. This figure also makes it clear that seeding the surface has not led to the suppression of these small-scale waves.

3.2. *Wave measurements*

A spectrogram of the surface slope measured by the LSG is shown in figure 4 for a final wind speed of 3 m s^{-1}. The first waves are detected at 15–20 s with a dominant frequency of approximately 9 Hz. The bandwidth of the spectrum is limited between 5 and 15 Hz initially, but increases rapidly to both higher and lower frequencies around 40 s. The peak of the spectrum shifts to lower frequencies as the waves transform from a duration-limited to a fetch-limited state. The peak of the spectrum stabilizes at an equilibrium frequency of 4.5 Hz after 70 s. Cuts through the spectrogram are shown as individual spectra averaged over 4 s and centred at 40, 45, 55, 65, and 75 s. The change in slope from approximately -3.5 to -10, or the 'cut-off' between 50 and 60 Hz is consistent with observations of Jähne & Riemer (1990) and Klinke (1996),

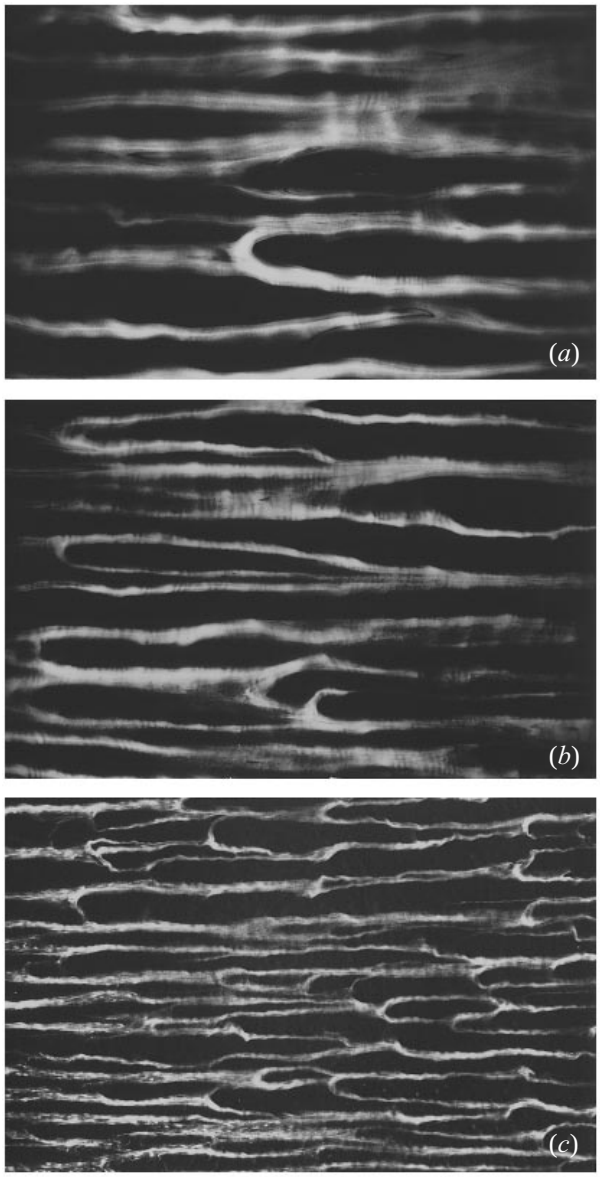

FIGURE 3. Flow visualization of the surface at a comparable stage in the evolution of the LCs (cf. figure 2 *d*, *e*) for the three final wind speeds: (*a*) 3; (*b*) 4; (*c*) 5 m s^{-1}. Each image represents an area of 85 cm $\times$ 57 cm. Note the reduction in scale of the LCs with increasing wind speed and the rich structure of bifurcations or dislocations in the streaks. Note in (*a*) and (*b*) the small-scale parasitic capillary waves with lengths of $O(1)$ cm.

and with a recent model of Fedorov & Melville (1998) and laboratory measurements of parasitic–capillary waves by Fedorov, Melville & Rozenberg (1997).

The corresponding spectrogram and spectra for the wire wave gauge measurements of the surface displacement, now at a final wind speed of 5 m s^{-1} (cf. figure 2), are shown in figure 5. The wire wave gauge does not have the high-frequency response of the LSG, and the spectra are truncated at 30 Hz. At this higher wind speed there is no initial period of limited bandwidth and the waves are almost immediately

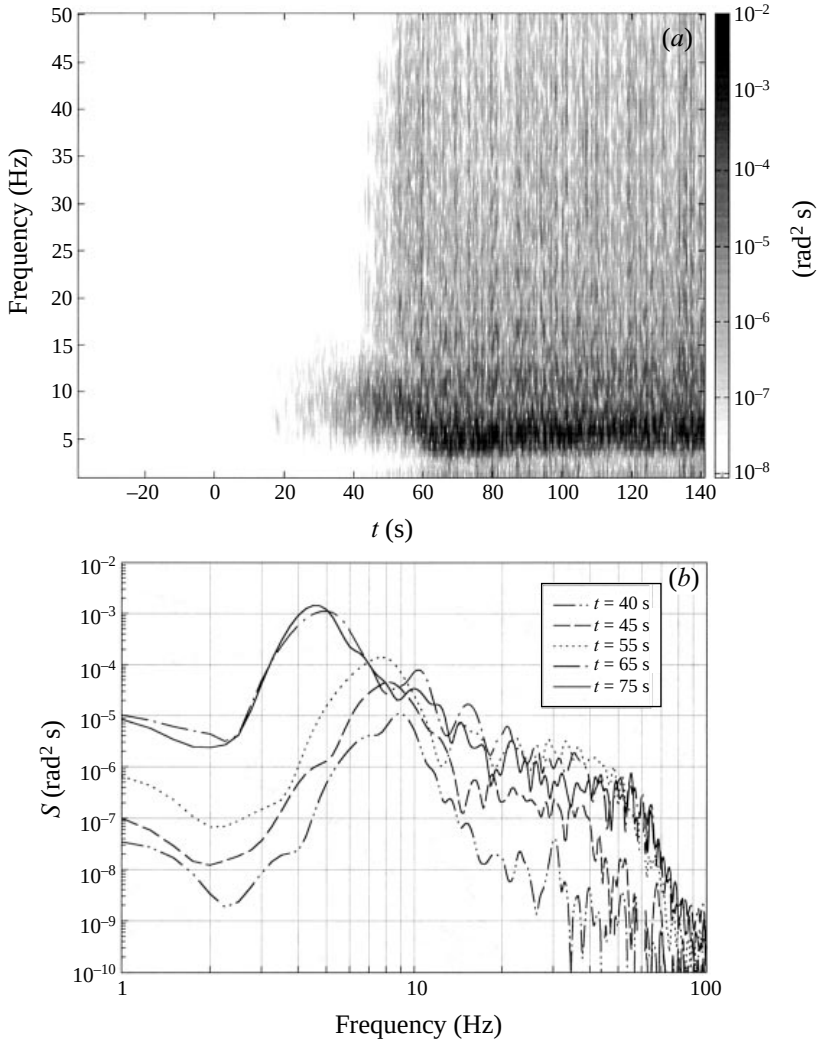

FIGURE 4. (*a*) Spectrogram of the surface slope measured with the laser slope gauge for a final wind speed of 3 m s^{-1}. Surface waves of limited bandwidth around a peak of approximately 9 Hz first appear above the noise at 5–20 s. Then the spectrum rapidly broadens and the the peak evolves from duration-limited waves to fetch-limited waves with a final peak frequency of 4.5 Hz. (*b*) Corresponding slope spectra averaged over 4 s at various times in the interval 40–75 s. Note the cut-off at 60 Hz.

broadbanded. (Due to the method of mounting, the wave gauge measurements also display some small vibrational noise at frequencies around 2 and 6 Hz, which clearly precedes the onset of the waves.) Again the spectrogram and individual spectra show a transition from duration-limited to fetch-limited states, with a high-frequency slope of approximately −4. The spectra compare favourably with those of Kawai (1979) who measured the initial growth of wind waves in a smaller wind-wave channel at shorter fetches and a wind speed of 5.1 m s^{-1}.

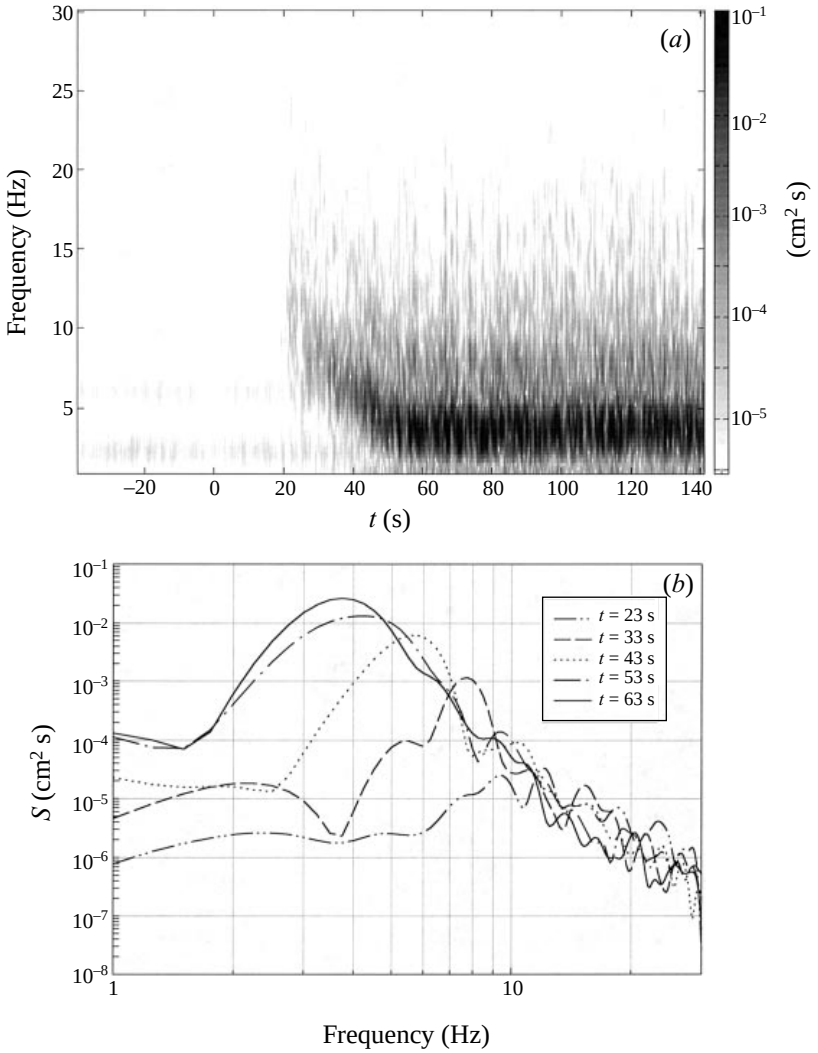

FIGURE 5. Wire wave gauge measurements of surface displacement for a final wind speed of 5 m s^{-1}. (*a*) Spectrogram of surface displacement. Due to the lesser sensitivity of the wave gauge when compared with the LSG, the spectra are truncated at 30 Hz. The bands around 2 and 6 Hz are vibrational noise that is approximately four orders of magnitude less than the spectral peaks. (*b*) Spectra averaged over 4 s at times in the range 23–63 s.

3.3. *Velocity measurements*

DPIV measurements of the evolution of the velocity and the transverse vorticity in a vertical longitudinal plane at a fetch of 13.34 m are shown in figure 6 at 5 s intervals from 46 to 71 s for a final wind speed of 3 m s^{-1}. The measurements begin at a depth of 2.7 mm, which is as close to the surface as the data could be processed while imaging total depths of $O(10)$ cm. The wind blows from left to right (cf. figure 1). These are 'instantaneous' fields obtained by processing images 15 ms apart. At 46 and 51 s the flow is almost plane parallel and confined to the first centimetre below the surface. The vorticity too is concentrated in the same region and, apart from the background noise, is everywhere positive. There is no significant wave activity, at least

in the measurable velocity field below 2.7 mm depth. At 56 s, waves of approximately 3 to 5 cm wavelength are apparent, and the positive vorticity has now extended to a depth of 2 cm. At 61 s the vorticity has extended down to depths of 4 cm and we see the first signs of significant negative vorticity. The perturbations at the base of the vortical layer are now comparable to the depth of the layer itself. At 66 and 71 s we see the continued deepening of the vortical layer to 8 cm. The regions of large positive vorticity have been reduced significantly and the surface waves are now longer, around 7–8 cm in length.

To obtain measurements of the horizontal velocity as a function of time, DPIV measurements from images similar to those in figure 6 were averaged over one second and then averaged horizontally over the width of the image (17.3 cm) to provide vertical profiles of the horizontal velocity as a function of time starting at a depth of 2.7 mm below the surface. Figure 7 shows an example for a final wind speed of 3 m s^{-1}. Up to approximately 56 s, the evolution of the surface shear layer is composed of a monotonic increase in the maximum velocity and a monotonic deepening of the layer. Simple scaling based on a balance between acceleration of the water and the gradient in the viscous stress implies that the depth of the layer should increase as $(\nu t)^{1/2}$, where ν is the kinematic viscosity. After 56 s this would give a depth of $O(1)$ cm, consistent with the measurements. To test this scaling, the inset in figure 7 shows the data from 21 to 56 s, plotted as $\tilde{u} = u/u(z^* = 0.59)$ versus $z^* = z/(\nu t)^{1/2}$. The value of the normalized depth $z^* = 0.59$ was chosen as the minimum depth (2.7 mm) at the minimum time (21 s) for this sequence. The data collapse quite well, certainly well enough for scaling purposes, and well enough to confirm that vertical transport of horizontal momentum is *not* due to an enhanced turbulent transport prior to the onset of instability between $t = 56$ and 61 s.

Up to $t = 56$ s the velocity closest to the surface (2.7 mm depth) is accelerating, although it should be cautioned that the velocity at the surface, which may be much larger than that at 2.7 mm depth, is not resolved by these DPIV measurements. The spatial resolution of the DPIV measurements, which determines how close to the surface the velocity can be measured, was dictated by the need to resolve the larger-scale mixing associated with the penetration of LCs and turbulence. Estimates of the surface velocity from flow visualization similar to figure 2 demonstrate that prior to the development of the LCs, the surface velocity may be significantly greater than that at 2.7 mm. (See below.) Around 56 s the velocity at the level closest to the surface reaches a maximum and then decreases as the momentum near the surface is mixed down by the evolving LCs and turbulence. Over the space of 20–25 s the momentum in the upper 2 cm (and the vorticity, cf. figure 6) is rapidly mixed down to a depth of approximately 8 cm. The velocity profile at $t = 81$ s, with a local maximum, or 'jet', at around $z = 5.5$ cm was commonly observed in these measurements, and is qualitatively similar to profiles computed by Leibovich (1977, figures 3, 4) and Leibovich & Paolucci (1980, figures 3, 16). Indeed, the evolution of these velocity profiles prior to $t = 81$ s is qualitatively very similar to Leibovich & Paolucci (1980, figure 16*d*).

Ensemble averages over three realizations of the development of the wind speed, r.m.s. wave slope, and the near-surface velocity in the water for three final wind speeds ($U = 3$, 4, 5 m s^{-1}) are shown in figure 8. The near-surface DPIV velocity data are those at 2.7 mm depth, similar to those in figure 7. Stages in the evolution of the surface wave field, as shown in the spectrograms of the laser slope gauge data in figure 4 are denoted by the horizontal bar at the bottom of each panel. The dotted bar corresponds to the initial generation of surface waves of limited bandwidth in

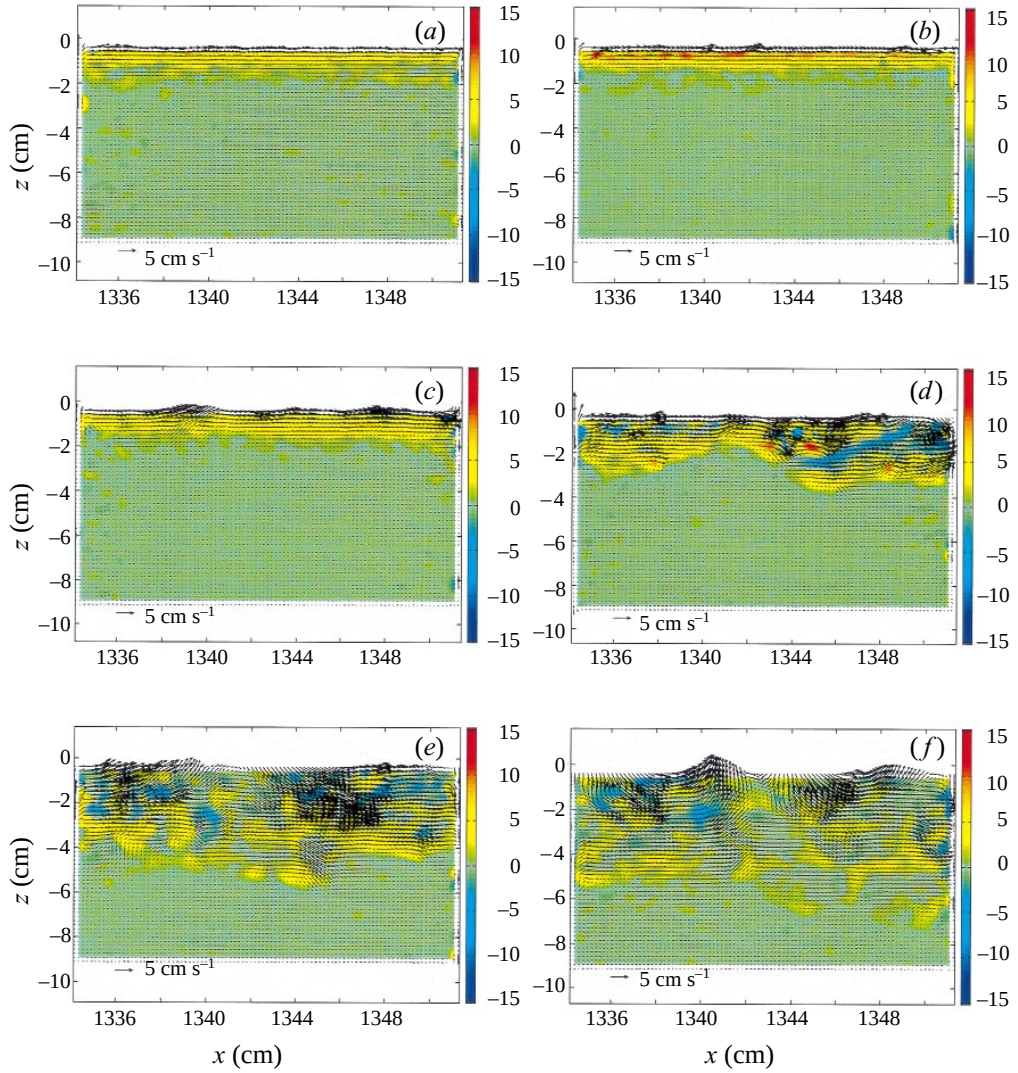

FIGURE 6. Longitudinal DPIV measurements at a fetch of 13.34 m for a final wind speed of 3 m s^{-1} at 5 s intervals from 46 to 71 s. The velocity vectors are shown along with colour contour plots of the transverse vorticity component. The vorticity scale is in s^{-1}. The minimum depth of the DPIV measurements is 2.7 mm. Note that the influence of the surface waves below the minimum depth of the measurements is first seen at $t = 56$ s. Note the large fluctuations in the base of the vortical layer in (*d*).

the frequency domain. The solid bar is characterized by a broad-band wave field whose slope-spectrum peak evolves to a lower final equilibrium value, and is related to the evolution from a duration-limited to fetch-limited spectrum. The solid arrows at the bottom bound the stages in the initial evolution of the LCs which correspond to those shown in figure 2 for 5 m s^{-1}. In each case we see that the growth of the waves lags the development of the wind-driven surface shear layer, consistent with the DPIV images which show that there is very little wave growth during the initial acceleration of the almost-planar surface. The implication of this observation is that the initial momentum flux from wind to water is almost exclusively into the surface

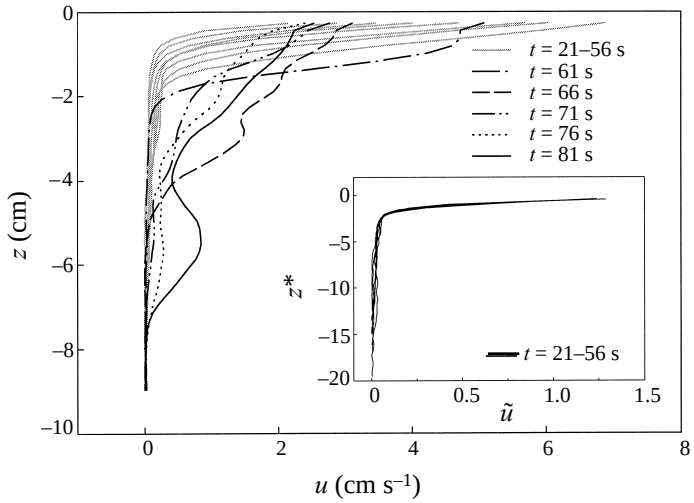

FIGURE 7. Horizontal velocity profiles, for a final wind speed of 3 m s^{-1}, obtained by averaging across images comparable to those in figure 6 for a period of 1 s. Up to 56 s the profiles correspond to a monotonically accelerating and deepening shear layer. From 61 s to 81 s the surface velocity decreases as the momentum mixes down to a depth of 8 cm. The inset shows the data from $t = 21$–56 s, plotted as $\tilde{u} = u/u(z^* = 0.59)$ versus $z^* = z/(\nu t)^{1/2}$. The value of the normalized depth $z^* = 0.59$ was chosen as the minimum depth (2.7 mm) at the minimum time (21 s) for this sequence.

current. The r.m.s. wave slope increases due to both local growth of the waves and propagation downstream of waves from shorter fetches.

At the lower wind speeds the development of significant LCs occurs near the maximum in the near-surface velocity. This is less clear at the highest wind speed in which the velocity maximum lasts longer. It is important to note that the time scales for the evolution of the near-surface current and surface waves are comparable, in contrast to the available LC theories and numerical modelling, which assume a homogeneous statistically stationary surface wave field. What is clear from the data, especially at the lower wind speeds, is that the rapid development of the LCs occurs in the neighbourhood of the maximum of the near-surface velocity, leading to vertical transport of momentum and a deceleration of the surface flow. This is apparent in figure 7.

Visualization of the surface showed that there were significant differences between the velocity measured at a depth of 2.7 mm and that at the surface. Figure 9 shows composite plots of the velocity profiles at the time of first observation of the streaks, with the velocity at the surface manually estimated from surface flow visualization, and that at depths greater than 2.7 mm measured with DPIV. Since the particles at the surface are drawn into surface jets with velocities greater than the surface mean velocity, care must be taken to avoid biases in estimation of the surface velocity. These difficulties precluded the use of standard DPIV processing to measure the surface velocity, and the error bars are correspondingly larger. Notwithstanding these difficulties, it is clear that much of the velocity difference between the surface and deeper water is contained in the first few millimetres, at least until the onset of LCs.

3.4. *Streamwise vorticity*

While the flow visualization of the surface (figure 2) provides circumstantial evidence for the development of LCs, the real test is whether the surface streaks are associated

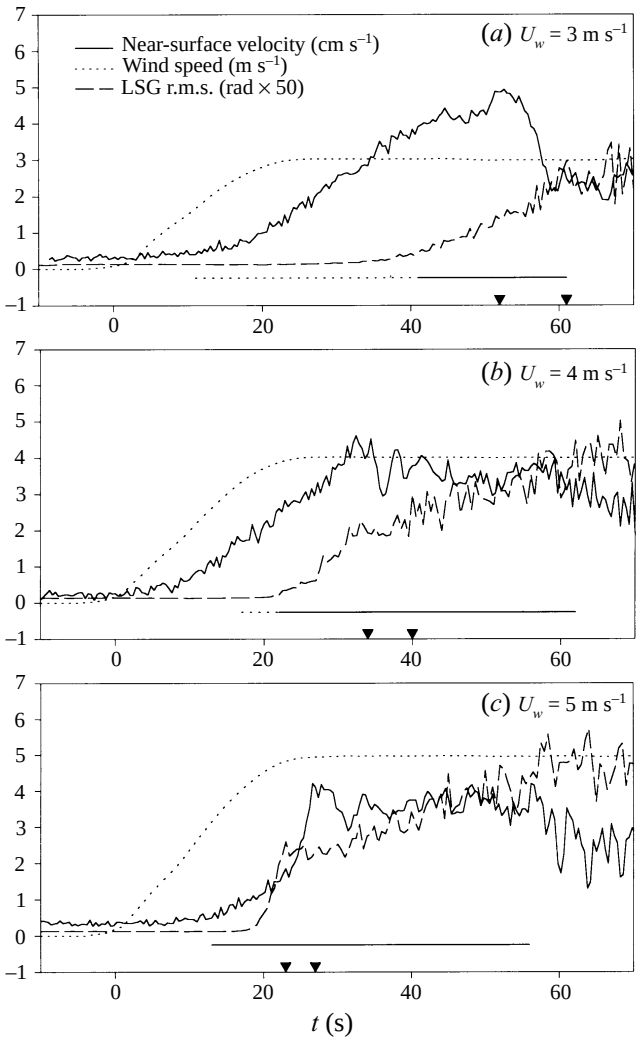

FIGURE 8. A summary of the evolution of the wind speed, the near-surface velocity (at 2.7 mm), and the r.m.s. surface slope for the three wind speeds. The data are ensemble averaged over three runs at each wind speed. The arrows at the bottom of each frame bound the stages in the evolution of the initial LCs represented by those shown in figure 2. The dotted horizontal bar corresponds to the initial generation of surface waves of limited bandwidth in the frequency domain. The solid bar is characterized by a broad-band wave field whose slope-spectrum peak evolves to a lower final equilibrium value, and is related to the evolution from a duration-limited to fetch-limited spectrum. In each case there is a significant lag between the onset of the wind and the growth of the waves. The initial growth and evolution of the LCs occurs during the time that the wave field is also evolving. The peak in the surface velocity occurs in the neighbourhood of the time at which the LCs first appear.

with longitudinal (streamwise) vorticity. To answer this question, DPIV measurements of velocities and vorticity in the cross-wind (transverse) plane were made at the same fetch and for the same final wind speed (3 m s^{-1}) as the longitudinal velocity field of figure 6. Figure 10 shows a sequence of velocity vectors and contour plots of longitudinal vorticity that is generated near the surface and transported into the interior of the water column. (Note that figure 2 and figure 10 do not come from

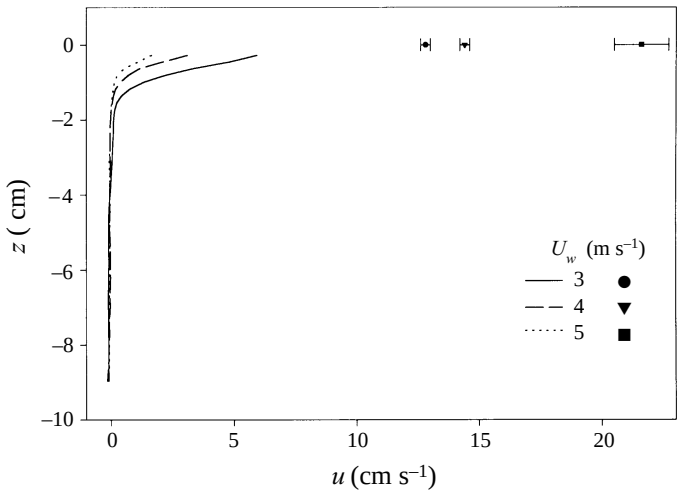

FIGURE 9. Horizontal velocity profiles at the inception of the LCs for the three wind speeds. The continuous profiles below a depth of 2.7 mm are measured with automated DPIV. The velocities at the surface are determined from a combination of manually analysed flow visualization and DPIV.

the same realization of the flow.) The individual frames, which span only 1.66 s, are at times $t = 54.33$, 54.66, 54.99, 55.33, 55.66, and 55.99 s, and proceed from left to right and top to bottom. The graph at the top of each frame is the brightness (arbitrary scale) of the surface measured in the DPIV image. This is comparable to a measurement of the brightness along a vertical cut in a panel of figure 2. Larger values correspond to more particles at the surface, and, by implication, a region of convergence of the transverse surface velocity. Prior to development of the LCs the surface is continuously marked by particles in the DPIV image. These measurements clearly confirm that the generation of streamwise vorticity of both signs is associated with the surface streaks. The velocity vectors, which include both rotational and irrotational components, confirm that the horizontal velocity gradients at the surface are consistent with this interpretation. The sequence also shows that the development of the instability is at best only quasi-periodic, and that a number of vortical scales are rapidly generated.

The two-dimensional plots of vorticity (both transverse and longitudinal) can be squared, averaged horizontally, and then integrated vertically over the frame to give the depth-integrated mean-square vorticity, which is proportional to the enstrophy. In figure 11(*a*) the transverse depth-integrated mean-square vorticity is shown to grow slowly at first, consistent with the data of figure 6. The only exception to this is in the data for 5 m s^{-1}, where our inability to measure the vorticity all the way to the surface may be biasing the results. That is, vorticity generated very near the surface, at depths less than 2.7 mm, is not measured. The corresponding longitudinal depth-integrated mean-square vorticity is shown in figure 11(*b*). In contrast to 11(*a*), the enstrophy here grows very rapidly following the first visual signs of streaks which are marked with the arrows. It is clear that the surface streaks are an indicator of longitudinal vorticity in the water column. Also of interest in this figure is the fact that the rapid growth of the longitudinal vorticity is associated with local peaks in the transverse enstrophy, an indication of the rapid evolution of three-dimensional effects.

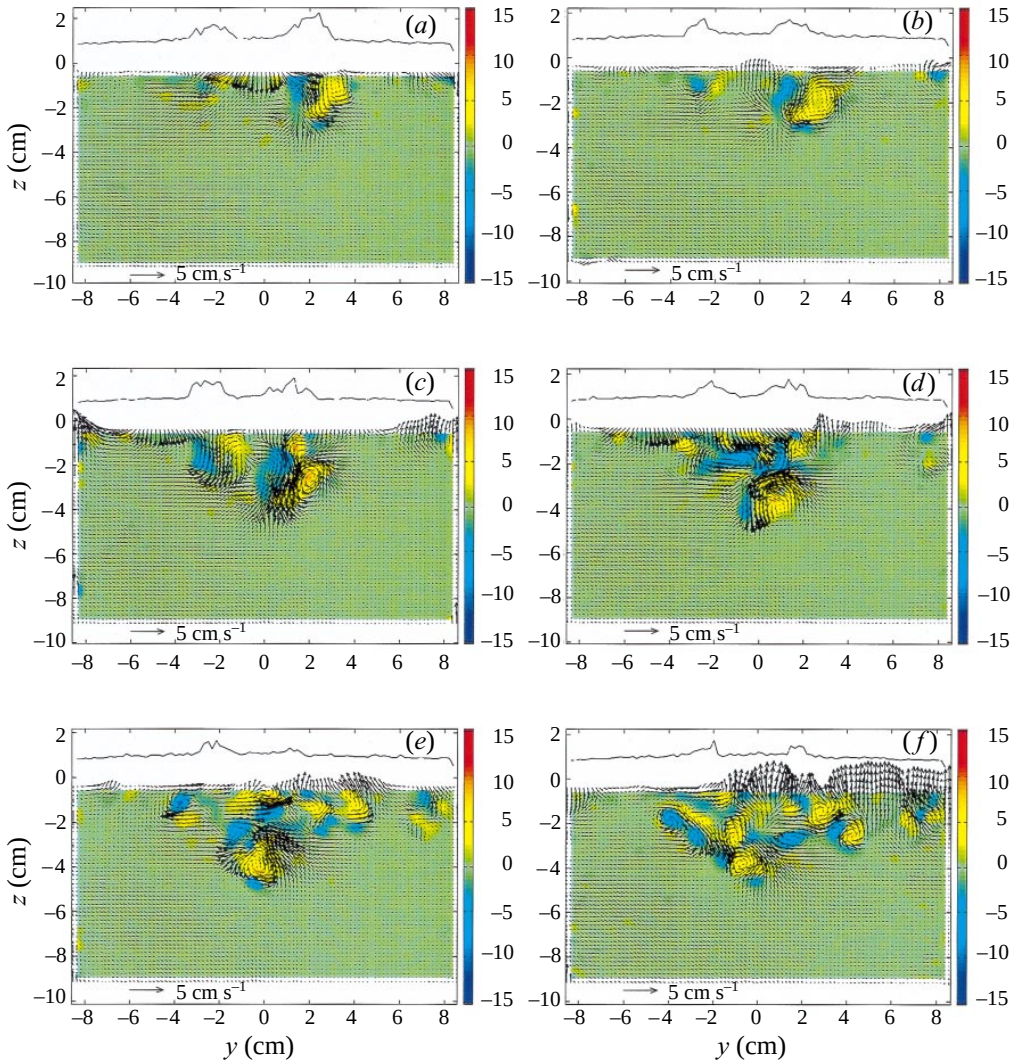

FIGURE 10. Transverse DPIV measurements at a fetch of 13.34 m for a final wind speed of 3 m s^{-1} at time intervals of 0.33 s from $t = 54.33$ to 55.99 s. The velocity field is shown by vectors and the longitudinal vorticity is colour contour plotted with the colour-bar scale in units of s^{-1}. The line at the top of each frame is the image intensity at the surface (arbitrary scale) so that streaks at the surface (regions of accumulation of seeding particles) are represented by an increase in intensity. This sequence shows what was initially a pair of dipolar regions of vorticity near the surface (with corresponding surface streaks) evolving and mixing down into the water column.

3.5. *Initial scales*

In order to compare the measurements with available theories of LC generation, we have measured various scales at the onset of the surface streaks. These are shown in figure 12. The length scales for the waves and the streak spacing were determined by peak counting and by spectral methods. Cuts along (for the waves) and across (for the streaks) images such as those shown in figure 2 (typically 4 to 6 in each direction) were made and peaks in optical intensity were counted. Two-dimensional spectra of the images were also computed and the wavenumbers of the relevant peaks were

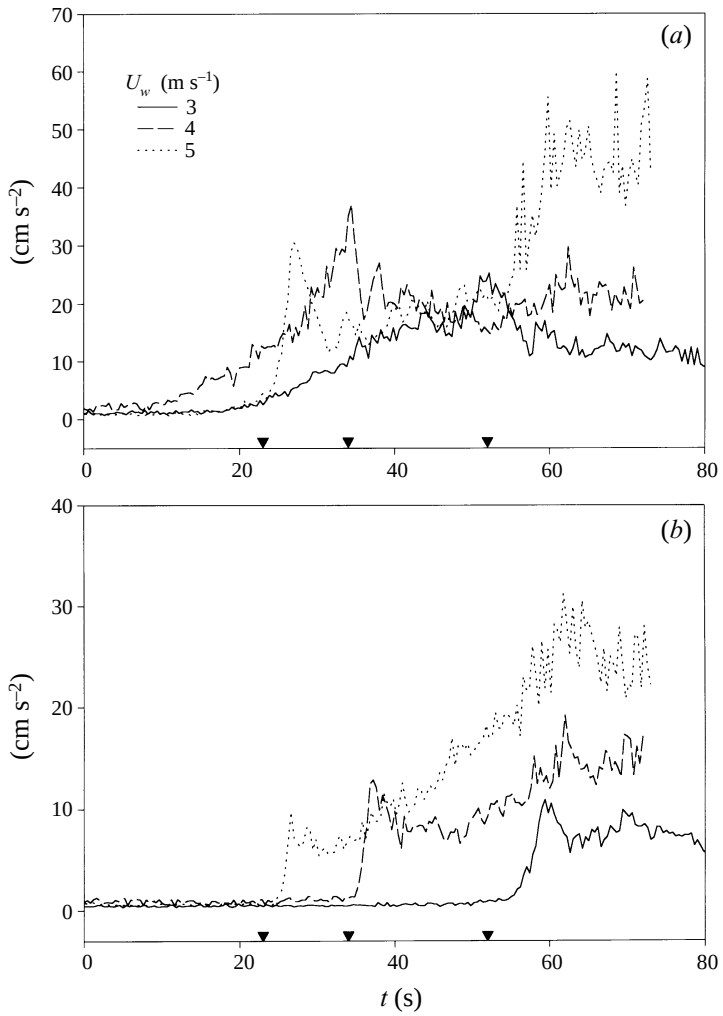

FIGURE 11. Depth integral of the mean-square vorticity averaged horizontally over the DPIV images (cf. figures 6 and 10), and over 0.3 s, plotted as a function of time: (*a*) transverse component; (*b*) longitudinal component. The arrow heads at the bottom of each figure mark (in increasing time) the inception of Langmuir circulations for 5, 4, and 3 m s^{-1}, respectively. The levels at $t = 0$ are representative of the noise due to residual motions in the channel.

measured. Since the images are not optically calibrated, and since the phenomena are not strictly linear, the error bars on these measurements are not small. The depth of the surface shear layer was determined from data like those in figure 7 by estimating the depth of the point of maximum curvature in the velocity profile. The streak spacing and the surface wavelength are comparable and decrease with increasing final wind speed. In contrast, the shear layer depth does not vary much across the range of the experiments. It is important to note that all of these scales are very much smaller that the width of the channel (2.39 m), the depth of the water (1.17 m), the height of the airstream (1.27 m) and the fetch (12–13 m). This distinguishes these experiments from earlier attempts to measure LCs in the laboratory.

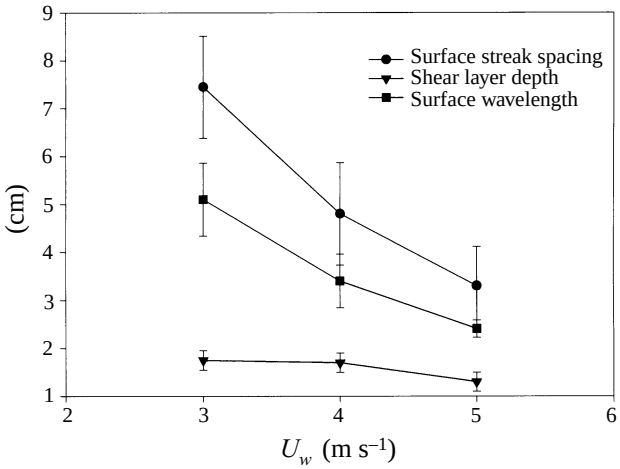

FIGURE 12. Measurements of the surface wavelength, the surface streak spacing and the depth of the shear layer at the inception of the Langmuir circulations.

4. Comparison with theory

As far as we are aware there is no available theory nor numerical predictions of instability to LCs that are directly applicable to the conditions of the experiments. However, for reasons of completeness, it is worthwhile to state just what those conditions are, and, where possible, to compare with related predictions.

4.1. *The surface shear layer*

Firstly, it is important to establish that the phenomena observed in these experiments are transitional, with the waves and the LCs being generated on a laminar shear flow in which the effects of turbulence are initially negligible.

Due to the acceleration of the airflow it is not possible to simply state the boundary conditions at the surface and therefore a simple complete prediction of the initial evolution of the velocity field is not possible. However, given the apparent success of the scaling of the depth of the current, it did seem worthwhile to test just how well the surface current could be predicted with a simple viscous model. This is a very important point, because if we can be sure that the transport was predominantly viscous prior to the onset of LCs then we will be able to test theories of LC generation without recourse to *ad hoc* turbulent closures or intensive DNS or LES. In principle, a simple viscous model would also permit the extrapolation of the subsurface velocity measurements to the surface.

Consider the evolution of a thin plane surface shear layer in an unbounded quiescent liquid driven by an airflow above. With the boundary layer approximation that streamwise scales are much larger than the transverse scale, the governing equations for an incompressible fluid are

$$\frac{\partial u}{\partial t} + u\frac{\partial u}{\partial x} + w\frac{\partial u}{\partial z} = -\frac{1}{\rho_w}\frac{\partial p}{\partial x} + \nu\frac{\partial^2 u}{\partial z^2}, \tag{4.1a}$$

$$\frac{\partial p}{\partial z} = 0, \tag{4.1b}$$

$$\frac{\partial u}{\partial x} + \frac{\partial w}{\partial z} = 0, \tag{4.1c}$$

with

$$u = U_w(x,t), w = 0 \quad \text{at} \quad z = 0, \tag{4.1d}$$

$$u, w \to 0 \quad \text{as} \quad z \to -\infty, \tag{4.1e}$$

and the streamwise pressure gradient is assumed given.

From equation (4.1*b*), the streamwise pressure gradient in the water matches that in the air, but the ratio of the densities of air and water is $O(10^{-3})$, in consequence of which the pressure gradient in the liquid may be neglected to leading order. For the measurements in question $u = O(10)$ cm s^{-1}, the time scale for evolution of the flow is of order 10 s, and the fetch, x, is $O(10)$ m. With these scales, the primary balance is between the unsteady term and the viscous term and to leading order the equations reduce to

$$\frac{\partial u}{\partial t} = \nu \frac{\partial^2 u}{\partial z^2} \tag{4.2a}$$

with

$$u(z,t) = 0 \quad \text{for} \quad t < 0, \tag{4.2b}$$

$$u = U_w(t) \quad \text{at} \quad z = 0, \tag{4.2c}$$

and

$$u \to 0 \quad \text{as} \quad z \to -\infty. \tag{4.2d}$$

It may be shown that there is a similarity solution to this problem if and only if U_w varies as a power of t (Sherman 1990). For $U_w = At, A$ constant, the solution is

$$u(z,t) = At((1 + 2\eta^2)\,\mathrm{erfc}(\eta) - \frac{2}{\pi^{1/2}}\eta \exp(-\eta^2)) \tag{4.3}$$

where $\eta = -z/2(\nu t)^{1/2}$ for $z < 0$.

If U_w takes a more general form, equation (4.2) may be solved using Laplace transform techniques, giving a solution that can be expressed as a convolution integral with respect to time. To simulate the data in figure 8, especially 8(*a*), we set

$$U_w = A(1 - \cos \Omega t) \quad \text{for} \quad 0 < t < \frac{\pi}{\Omega}, \tag{4.4a}$$

$$U_w = A \quad \text{for} \quad t > \frac{\pi}{\Omega}, \tag{4.4b}$$

where Ω is chosen to fit the near-surface velocity data of figure 8. (Note that the origin of time here is not necessarily the same as that of figure 8. For example, the effective origin of time of the surface velocity for figure 8(*a*) is approximately 10 s.) The solution is

$$u(z,t) = A\mathrm{erfc}\left(\frac{z}{2(\nu t)^{1/2}}\right) - A\int_0^t \cos(\Omega(t-\zeta))\frac{z}{2(\nu\pi\zeta^3)^{1/2}}\exp(-z^2/4\zeta\nu)\mathrm{d}\zeta. \tag{4.5}$$

The first term is just the solution to the classical Rayleigh problem, while the second term accounts for the finite acceleration of the surface. The form of the second term clearly precludes the existence of a similarity solution in terms of $z/2(\nu t)^{1/2}$.

Figure 13 shows the similarity solution (4.3) and the more general solution (4.5) compared with the data from figure 7 for the 3 m s^{-1} case. The similarity solution, figure 13(*a*), is shown along with the data from figure 7 for times in the range 21–56 s. The similarity solution was obtained using a linear fit to the near-surface velocity

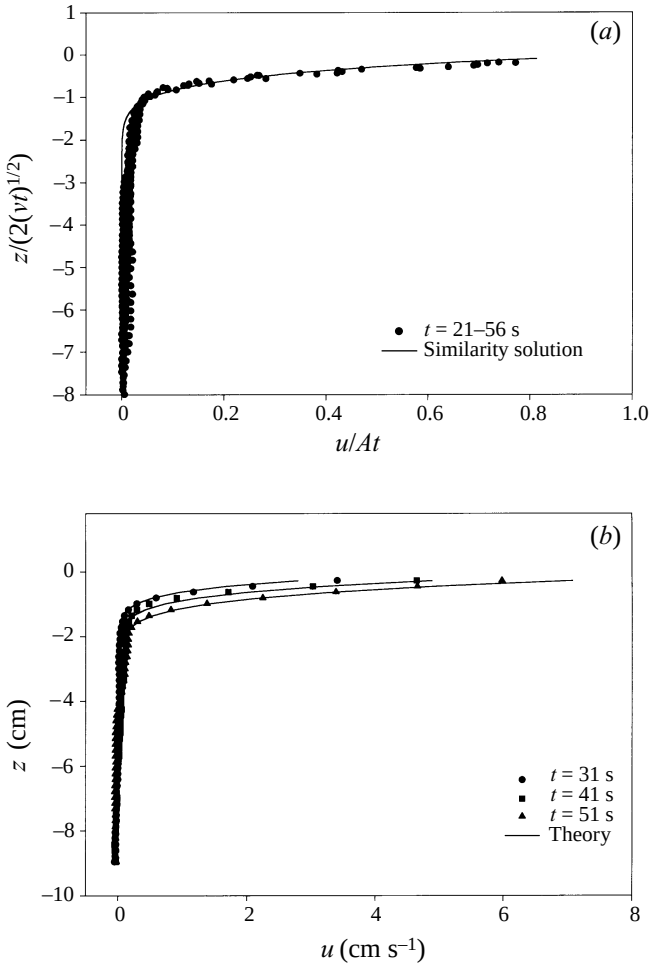

FIGURE 13. Comparison of measured velocity profiles prior to the inception of LCs for a 3 m s^{-1} final wind speed. (*a*) The similarity solution from equation (4.3) for $u(0,t) = At$. (*b*) The solution for a sinusoidally increasing wind speed at the surface from equation (4.5).

curve in figure 8(*a*). The agreement is very good except in the neighbourhood of the maximum curvature of the profile, and some of that discrepancy may be due to the residual currents in the channel. In figure 13(*b*) we display the more general solution where now the near-surface velocity in figure 8(*a*) has been fitted with a sinusoidal curve. The agreement with the data is comparable to that for the similarity solution. So, while a similarity solution does not strictly apply to the conditions of the experiment, it appears to do a good job in fitting the velocity profile data.

More general unsteady boundary layer solutions may apply at different fetches and for different rates of acceleration of the wind, and recent work by Phillips (1996) may be relevant in those cases.

4.2. *Comparison with LC stability theory*

While there is no theory nor numerical predictions that are completely compatible with the conditions of the experiments, it is worth comparing the measurements, especially the scales of the initial LCs, with the available predictions of instability.

Leibovich & Paolucci (1981) considered the initial boundary-value problem of an existing homogeneous stationary wave field subject to a wind beginning at some initial time with a constant stress. They presented a stability diagram for LCs of dimensionless transverse wavenumber $k_{lc}^{*} = k_{lc}/k$ versus La^{-1}, where k is the characteristic wavenumber of the surface waves and La is the Langmuir number, which represents the ratio of the diffusion of streamwise vorticity to the production of streamwise vorticity by the effects of the Stokes drift. Specifically, the Langmuir number is defined to be

$$La = \left(\frac{\nu^3 k^2}{\sigma a^2 u_{*w}^2} \right)^{1/2}, \tag{4.6}$$

where ν is the kinematic viscosity (usually an 'eddy' viscosity), σ is the radian frequency of the waves, a is the wave amplitude, and u_{*w} is the friction velocity in the water. The reciprocal of the Langmuir number is the analogue of the Rayleigh number in convection, with the flow tending to be globally stable for small La^{-1}, with a most unstable wavenumber for linear perturbations as La^{-1} increases above the global stability boundary. The basic tests of the theory concern the predictions of the global stability boundary and the most unstable wavenumber. As in thermal convection, finite-amplitude effects are expected to rapidly exceed the assumptions of the linear stability theory.

For our purposes it is convenient to rearrange equation (4.6) in terms of variables that are either directly measured or reliably inferred from the measurements. Thus we write

$$La^2 = \frac{\nu^3 k^3}{(\sigma/k)(ak)^2 u_{*w}^2}. \tag{4.7}$$

Since the velocity profiles in the surface shear layer scale with the (molecular) kinematic viscosity, we are free of the assumptions of an eddy viscosity. We measure k (see § 3.5), and using the linear dispersion relationship for irrotational gravity–capillary waves,

$$\sigma^2 = gk \left(1 + \frac{Tk^2}{g} \right), \tag{4.8}$$

where T is the surface tension coefficient, and g is the gravitational acceleration, can infer σ. We also measure the phase speed of the waves, including the Doppler shift, directly. The component of the wave slope along the channel is directly measured with the LSG, and we set the characteristic value of ak equal to $\sqrt{2}(ak)_{rms}$, with the r.m.s. values taken from figure 8. The friction velocity in the water is estimated from the assumption that the drag coefficient of the water on the airflow is 1.1×10^{-3} (Komen *et al.* 1994). We attempted to extrapolate the profiles shown in figure 13 to the surface, but except for the 3 m s^{-1} case, the velocity estimates at the surface were significantly smaller than those measured. We attributed this to the difficulty of determining the exact location of the surface and the large velocity gradients there. Similar difficulties arose in trying to use the theoretical profiles to infer the surface stress and hence u_{*w}.

Table 1 collects all the measured parameters at the time of the first observation of the streaks at the surface. The measured values represent ensemble averages over three realizations of each experiment. Because the speed of the current is comparable to the phase speed, there is a significant difference between the values of σ/k, inferred from k, and the measured phase speed. Also, it is not clear that the waves are irrotational; however, the effect of the differences between the inferred and measured phase speeds

Wind speed (m s^{-1})	Time (s)	λ_w (cm)	λ_{lc} (cm)	LSG rms (rad)	Surface wave phase speed (cm s^{-1})	σ/k (cm s^{-1})	Surface velocity (cm s^{-1})	k^*_{lc} [mean]	La^{-1} [mean]
3	52	5.1±0.8	7.5±1.1	0.030	34.2±5.2	29.8±6.6	12.4±0.8	0.68±0.20	59±26
4	34	3.4±0.6	4.8±1.1	0.038	30.4±4.0	25.8±6.2	14.1±1.0	0.71±0.36	50±26
5	23	2.4±0.2	3.3±0.8	0.049	40.6±3.2	24.8±2.7	18.4±1.2	0.72±0.23	46±11
								[0.68±0.24]	[52±21]

TABLE 1. Measured and inferred parameters at the inception of the Langmuir circulations for the three wind speeds. Time is the inception time; λ_w, the surface wavelength; λ_{lc}, the wavelength of the LCs; σ/k, the irrotational surface wave phase speed.

is within the stated errors in La^{-1}. It is notable that the observed 'most unstable' wavenumber, k^*_{lc}, is effectively constant across the range of the experiments. This is apparent from figure 12 where it can be seen that the ratio of the surface streak spacing to the surface wavelength is approximately constant. However, the relatively large error bars and the limited range of experimental conditions suggest caution in interpreting this result. The values of La^{-1} at instability are in the range 46 to 59 with error bars that are larger than this difference. This implies that over the range of conditions for these experiments, instability to LCs occurred at a fixed reciprocal Langmuir number, 52±21, and fixed dimensionless wavenumber, 0.68±0.24, albeit with large error bars. (These mean values have been based on averages of the upper and lower bounds for each parameter over the three wind speeds.) This suggests that the Langmuir number is an appropriate control parameter. The most unstable wavenumber is approximately twice that predicted by Leibovich & Paolucci (1981), and the reciprocal Langmuir number is one to two orders of magnitude greater than their prediction which is shown in figure 14. The data suggest that this flow is more stable to LCs than that considered by Leibovich & Paolucci (1981). What is the cause of the discrepancy?

There are a number of ways in which the experiments differ from the assumptions of the theory. Firstly, the current at instability is not weak, not $O((ak)^2)$, when compared with the phase speed of the waves. Rather, it is comparable to the phase speed of the waves, and as Phillips and his colleagues (Phillips & Wu 1994; Phillips & Shen 1996), have shown for corresponding $O(1)$ *inviscid* flows, the additional effects may lead to a relative stabilization of the flow when compared with the case for weaker currents. Unfortunately, there are no predictions for the $O(1)$ *viscous* flows that could be compared with the measurements. Secondly, the assumption that the wave field is stationary is not satisfied in these experiments. Clearly, the time scale for the evolution of the wave field and that for the evolution of the LCs are comparable (see figure 8), and this has important implications not only for the study of LCs but also for our understanding of the initial generation and evolution of the short surface waves. Since the waves are growing, the vortex force implied by the Langmuir number at the first sign of instability is greater than that at earlier times. Thus, the flow appears more stable when characterized by La at instability.† To confirm this effect, using equation (4.7), we show in figure 15 the reciprocal Langmuir number as a function of time up to the first appearance of the surface streaks. What is clear from this figure is that in each case La^{-1} grows monotonically in time and the time scale for this growth, which is dominated by wave growth, is comparable to the time scale

† We thank an anonymous reviewer for this suggestion.

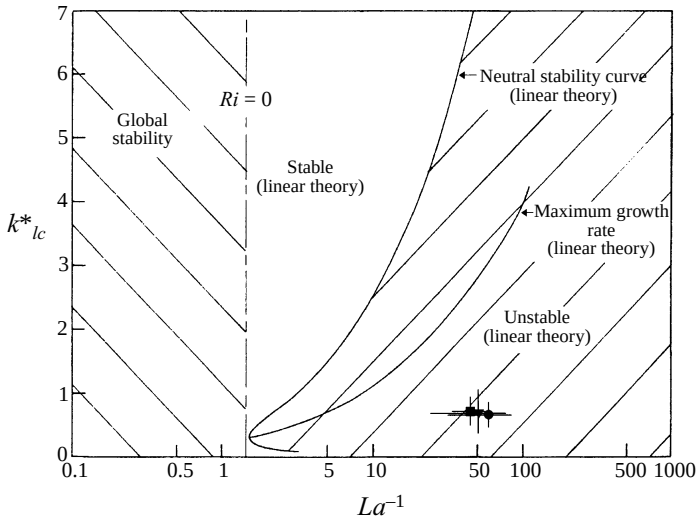

FIGURE 14. Comparison between the present measurements and the predictions of Leibovich & Paolucci (1981). The data are for the wavenumber and Langmuir number at LC inception: •, 3 m s^{-1}; ▾, 4 m s^{-1}; ■, 5 m s^{-1}.

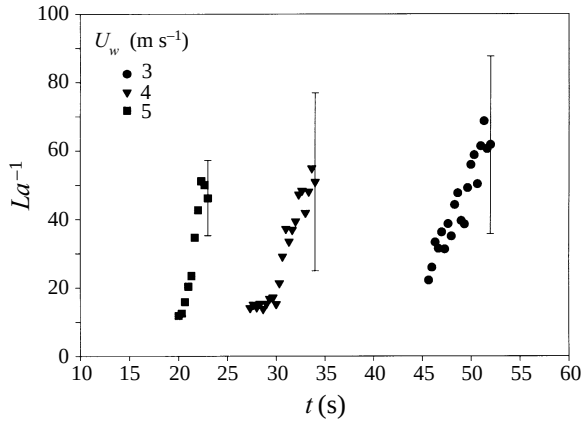

FIGURE 15. Time evolution of the reciprocal Langmuir number, computed from equation (4.7), prior to the inception of the LCs: •, 3 m s^{-1}; ▾, 4 m s^{-1}; ■, 5 m s^{-1}.

for the LCs to evolve from surface streaks to fully developed turbulent structures. (cf. figures 2 and 8). This implies that accurate measurement of the Langmuir number at instability may be very difficult.

5. Discussion

The primary results of this paper have been to demonstrate that LCs are generated shortly after the first appearance of surface waves on a wind-driven surface current, and to quantify the relevant scales. Over the range of experiments reported here, we have found that the initial instability to Langmuir circulations occurs at a reciprocal Langmuir number of 52 ± 21 and a dimensionless wavenumber of 0.68 ± 0.24. While there is a large literature on the initial generation of wind waves, and on the generation

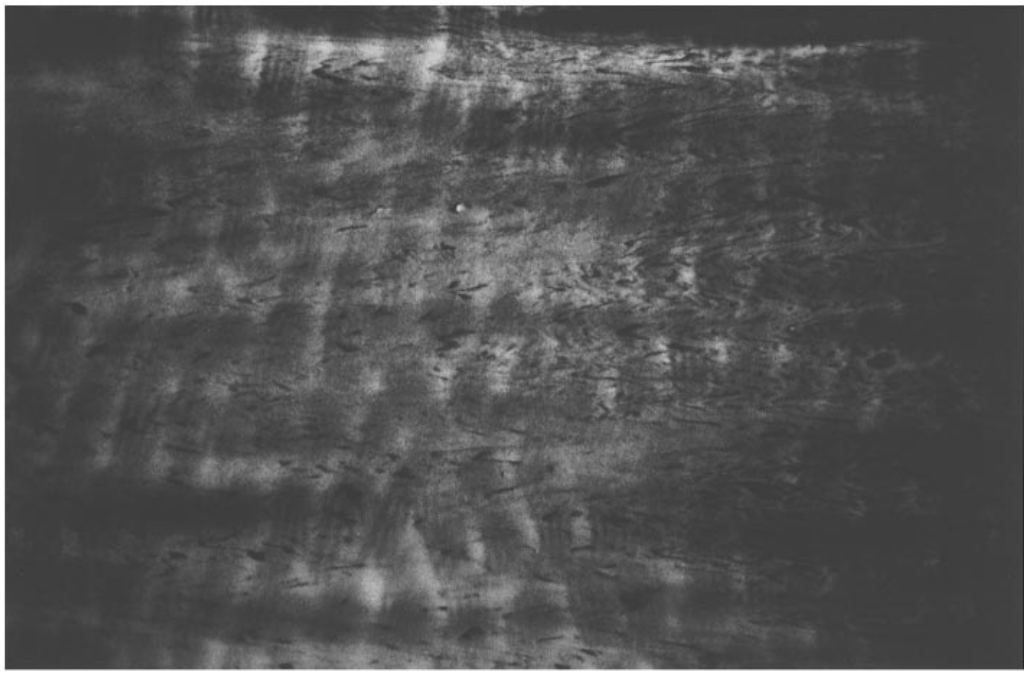

FIGURE 16. Flow visualization of the surface at $t = 32$ s for a final wind speed of 4 m^{-1}. The image represents an area of 85 cm $\times$ 57 cm. Note the bimodal directional pattern of the surface waves, and the deformation of small voids in the seeding showing evidence of modulations of the fluid velocity at the surface.

and evolution of LCs, it has not been fully appreciated that the two processes may occur over comparable time scales as instabilities of an accelerating surface shear layer. It is particularly important that LCs can now be studied as instabilities of a laminar flow without the unnecessary complication of a pre-existing turbulent field.

For application to the ocean and other larger water bodies it has been usual to concentrate on LCs of scales of $O(1$–$100)$ m, and some may question the relevance of these LCs having scales some two orders of magnitude smaller. However, their significance is underlined by figure 11 which shows that the mean-square vorticity associated with these small-scale LCs is of $O(1)$ s^{-2} when averaged over a depth of approximately 10 cm. Consider larger-scale LCs with lateral and vertical scales of $O(10)$ m and vertical velocities of $O(0.1)$ m s^{-1}, values associated with ocean observations (Weller & Price 1988). They will have a mean-square vorticity of $O(10^{-4})$ s^{-2}, when averaged over a depth of 10 m. Thus, if they were present all the time, the contribution of the small-scale LCs to the mean-square vorticity averaged over 10 m, would exceed that of the larger LCs by a factor of 10^2! We do not expect the small-scale LCs to be present all the time, but a factor 10^2 leads to the conclusion that their presence for only 1% of the time would be significant. Another reason for their significance is the presence of an inverse cascade that has been observed in numerical solutions and in these experiments (see figure 2). An improved understanding of the smaller scales of the motion is necessary to understand their evolution to larger scales.

Surface renewal models are commonly used to account for heat and gas flux across the air–sea interface, and are also useful in high-Rayleigh-number thermal convection. Such models assume an intermittent rapid disruption of the boundary layer at the

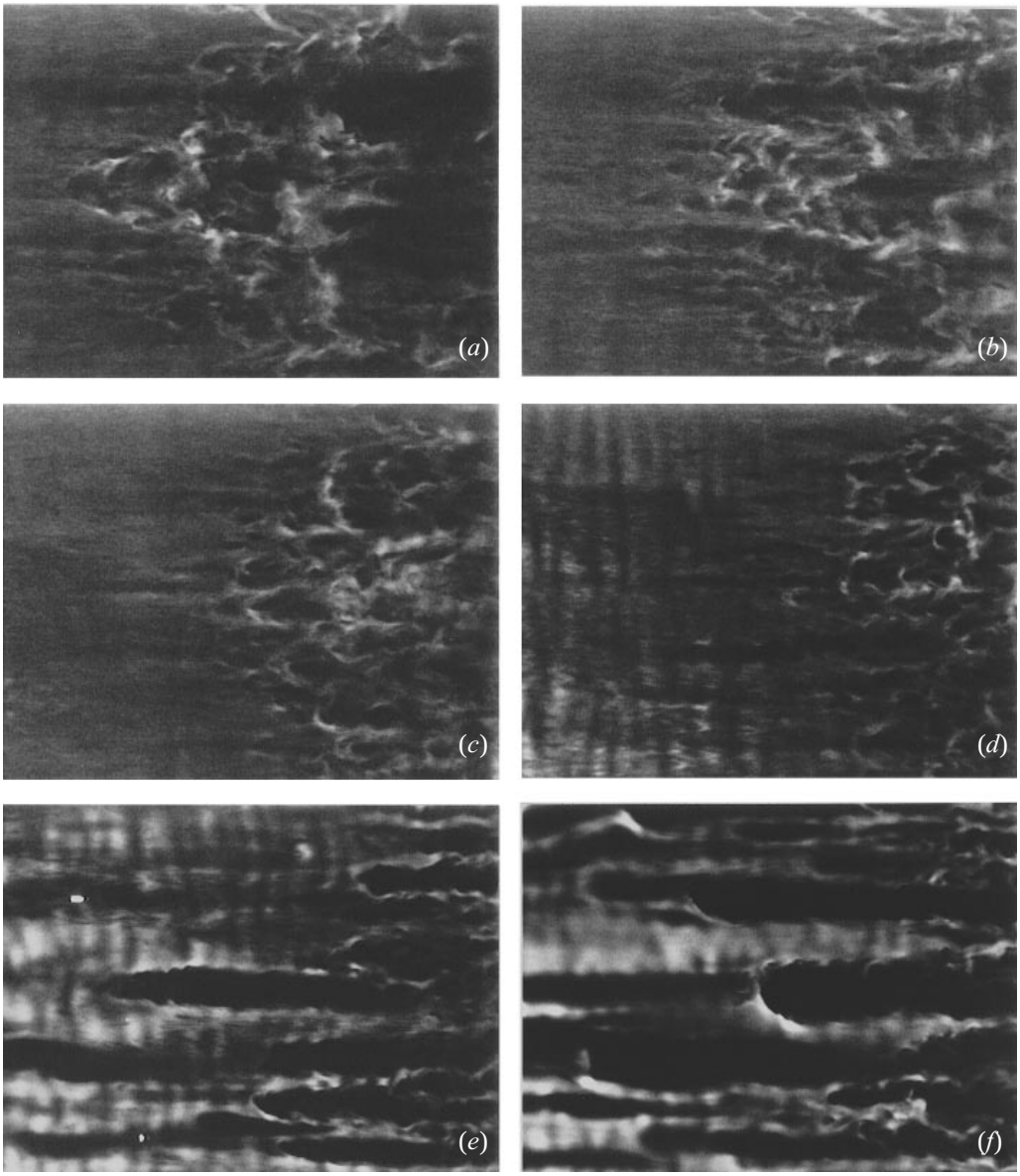

FIGURE 17. Visualization of the evolution of an instability at the surface as viewed from above for a final wind speed of 4 m s^{-1}. The flow is from left to right. The image size is 63 cm $\times$ 47.8 cm. Note the turbulent spot being swept down stream in (*a*) to (*d*), the surface waves following from upstream in (*d*) and (*e*), and the inception of Langmuir circulations (*e*), (*f*).

surface followed by a slower diffusive re-establishment of the layer. In the context of small-scale air–sea interaction, attention has focused on micro-scale breaking as the means by which the diffusive processes are disrupted. These results imply that the diffusive growth of the momentum (and thermal) boundary layer may also be unstable to LCs. Also, there are a number of interesting issues related to the transition from three-dimensional turbulence to quasi-two-dimensional turbulence in the neighbourhood of the air–water interface.

Finally, we present some flow visualization that conveys further evidence of the richness of this problem and the range of phenomena that may need to be addressed before a complete understanding of the instability of wind-driven surface shear layers to surface waves and LCs can be claimed.

Figure 16 is an example of a particle-seeded surface viewed from above for a final wind speed of 4 m s^{-1}. The photograph was taken shortly after the first evidence of LCs. What is striking about this image is the almost-bimodal directional pattern of the short waves, symmetric about the mean wind direction. This was unusual, with the great majority of surface images being represented by figures 2 and 3. Since the speed of the wind-driven current is comparable to the phase speed of the waves (see table 1), we were sensitive to signs of modulation of the waves by the LCs. Notice that the modulation of the velocity of the fluid at the surface is made evident by the deformation of small defects (voids) in the seeding which are generally consistent with an increase in the streamwise velocity in the streaks. Also, the existence of such a bimodal wave pattern prior to the formation of the LCs would be consistent with the so-called CL I mechanism of LC generation (Craik & Leibovich 1976; Leibovich 1983), which requires a transverse modulation of the Stokes drift to trigger the LCs. Unfortunately, we were not able to resolve whether the bimodal pattern was the cause or an effect of the LCs in these cases.

Figure 17 shows a sequence of images of the seeded surface seen from above for a wind speed of 4 m s^{-1}. The flow is from left to right. The first image in the sequence shows a transitional event that was seldom seen, but has the appearance of a turbulent spot in the water. Notice the characteristic V-shape pointing to the left. If it were the surface signature of a turbulent spot in the air it would have a V-shape pointing to the right, the direction of the airflow. However, in a frame of reference moving with the velocity at the surface the spot has the correct orientation for a turbulent spot in the water. Following the sequence of images, the spot evolves downstream with surface waves and LCs rapidly following behind. Indeed, there is some transverse structure associated with the spot, and this may provide another route for the onset of LCs. We emphasize that the appearance of a turbulent spot was very unusual and did not normally precede the appearance of surface waves and LCs. This is the only example found in approximately fifty individual runs of surface flow visualization.

We thank Horst Haußecker and Bernd Jähne who collaborated on the experiments in Delft that motivated this work (Haußecker *et al.* 1995), and kindly lent us the IR camera. We thank Anatol Rozenberg for the laser slope gauge measurements, and Charles Coughran and Mike Kirk, our colleagues at the Hydraulics Laboratory, Scripps Institution of Oceanography, for their support, especially in modifying the large wind-wave channel for these experiments. We are grateful to Mory Gharib and Chris Willert who introduced us to DPIV and to Florence Raynal whose review of the original version of this paper lead to significant improvements in the published version. This research was supported by grants from the National Science Foundation (OCE 9115944 & OCE9633794).

REFERENCES

Craik, A. D. D. 1977 The generation of Langmuir circulations by an instability mechanism. *J. Fluid Mech.* **81**, 209–223.

Craik, A. D. D. 1982*a* The generalized Lagrangian-mean equations and hydrodynamic stability. *J. Fluid Mech.* **125**, 27–35.

Craik, A. D. D. 1982*b* Wave-induced longitudinal-vortex instability in shear flows. *J. Fluid Mech.* **125**, 37–52.

Craik, A. D. D. & Leibovich, S. 1976 A rational model for Langmuir circulations. *J. Fluid Mech.* **73**, 401–426.

Faller, A. & Caponi, E. A. 1978 Laboratory studies of wind-driven Langmuir circulations. *J. Geophys. Res.* **83**, 3617–3633.

Farmer, D. M. & Li, M. 1995 Patterns of bubble clouds organized by Langmuir circulation. *J. Phys. Oceanogr.* **25**, 1426–1440.

Fedorov, A. V. & Melville, W. K. 1998 Nonlinear gravity-capillary waves with forcing and dissipation. *J. Fluid Mech.* **354**, 1–42.

Fedorov, A. V., Melville, W. K. & Rozenberg, A. 1997 An experimental and numerical study of parasitic capillary waves. *Phys. Fluids* (Submitted).

Gong, W. M., Taylor, P. A. & Dörnbrack 1996 Turbulent boundary-layer flow over fixed aerodynamically rough two-dimensional sinusoiidal waves. *J. Fluid Mech.* **312**, 1–37.

Haußecker, H., Shear, R. M., Jähne, B. & Melville, W. K. 1995 Horizontal and vertical spatial structures of turbulence beneath short wind waves. *Presented at XXI General Assembly IAPSO, Honolulu, August 1995.*

Jähne, B. & Riemer, K. 1990 Two-dimensional wave number spectra of small-scale water surface waves. *J. Geophys. Res.* **95**, 11531–11546.

Kawai, S. 1979 Generation of initial wavelets by instability of a coupled shear flow and their evolution to wind waves. *J. Fluid Mech.* **93**, 661–703.

Kenney, B. C. 1993 Observations of coherent bands of algae in a surface shear layer. *Limnol. Oceanogr.* **38**, 1059–1067.

Klinke, J. 1996 Optical measurements of small scale wind-generated water surface waves in the laboratory and the field. Dissertation, Universität Heidelberg.

Komen, G. J., Cavaleri, M., Hasselmann, K., Hasselmann, S. & Janssen, P. A. E. M. 1994 *Dynamics and Modelling of Ocean Waves.* Cambridge University Press. 532 pp.

Langmuir, I. 1938 Surface motion of water induced by wind. *Science* **87**, 119–123.

Leibovich, S. 1977 On the evolution of the system of wind drift currents and Langmuir circulations in the ocean. Part 1. Theory and the average current. *J. Fluid Mech.* **79**, 715–743.

Leibovich, S. 1983 The form and dynamics of langmuir circulations. *Ann. Rev. Fluid Mech.* **15**, 391–427.

Leibovich, S. & Paolucci, S. 1980 The Langmuir circulation instability as a mixing mechanism in the upper ocean. *J. Phys. Oceanogr.* **10**, 186–207.

Leibovich, S. & Paolucci, S. 1981 The instability of the ocean to Langmuir circulations. *J. Fluid Mech.* **102**, 141–167.

Leibovich, S. & Yang, G. 1998 Turbulent flow in natural water bodies driven by wind and surface waves. *J. Fluid Mech.* submitted.

Li, M., Zahariev, K. & Garrett, C. 1995 Role of Langmuir circulation in the deepening of the ocean surface mixed layer. *Science* **270**, 1955–1957.

McWilliams, J. C., Sullivan, P. P. & Chin-Hoh Moeng 1997 Langmuir turbulence in the ocean. *J. Fluid Mech.* **334**, 1–30.

Melville, W. K. 1996 The role of surface-wave breaking in air-sea interaction. *Ann. Rev. Fluid. Mech.* **28**, 279–312.

Melville, W. K. & Shear, R. 1996 Laboratory observations of Langmuir circulations. *Presented at XIXth Intl Congress of Theoretical and Applied Mechanics, Kyoto, August, 1996.*

Phillips, W. R. C. 1996 A class of unsteady boundary layers of finite extent. *J. Fluid Mech.* **319**, 151–170.

Phillips, W. R. C. & Shen, Q. 1996 On a family of wave-mean shear interactions and their instability to longitudinal vortex form. *Stud. Appl. Maths* **96**, 143–161.

Phillips, W. R. C. & Wu, Z. 1994 On the instability of wave-catalysed longitudinal vorticies in strong shear. *J. Fluid Mech.* **272**, 235–254.

Phillips, W. R. C., Wu, Z. & Jahnke, C. C. 1997 Longitudinal vortices in wavy boundary layers. In *IMA Conf Proc. on Wind-over Wave Couplings: Perspectives and Prospects.* Oxford University Press.

Phillips, W. R. C., Wu, Z. & Lumley, J. L. 1996 On the formation of longitudinal vortices in a turbulent boundary layer over wavy terrain. *J. Fluid Mech.* **326**, 321–341.

Plueddemann, A. J., Smith, J. A., Farmer, D. M., Weller, R. A., Crawford, W. R., Pinkel, R., Vagle, S. & Gnanadesikan, A. 1996 Structure and variability of langmuir circulation during the Surface Waves Processes Program. *J. Goephys. Res.* **101**, 3525–3543.

Sherman, F. S. 1990 *Viscous Flow*. McGraw-Hill 746 pp.

Skyllingstad, E. D. & Denbo, D. W. 1995 An ocean large-eddy simulation of Langmuir circulations and convection in the surface mixed layer. *J. Geophys. Res.* **100**, 8501–8522.

Smith, J. A. 1992 Observed growth of Langmuir circulation. *J. Geophys. Res.* **97**, 5651–5664.

Thorpe, S. A. & Hall, A. J. 1983 The characteristics of breaking waves, bubble clouds and near-surface currents observed using side-scan sonar. *Contin. Shelf Res.* **1**, 353–384.

Weller, R. A. & Price, J. F. 1988 Langmuir circulation within the oceanic mixed layer. *Deep-Sea Res.* **35**, 711–747.

Willert, C. & Gharib, M. 1991 Digital particle image velocimeter. *Exps. Fluids* **10**, 181–193.